



Photoelectrocatalytic N₂ fixation and C-H oxyfunctionalization driven by H₂O oxidation

Chang Hyun Kim^{a,1}, Jinhyun Kim^{a,b,1}, Frank Hollmann^c, Chan Beum Park^{a,*}

^a Department of Materials Science and Engineering, Korea Advanced Institute of Science and Technology (KAIST), 335 Science Road, Daejeon 305-701, Republic of Korea

^b Department of Chemical and Biomolecular Engineering, University of California, Berkeley, Berkeley, CA 94720, USA

^c Department of Biotechnology, Delft University of Technology, Van der Maasweg 9, 2629 Hz Delft, The Netherlands

ARTICLE INFO

Keywords:

Biocatalysis
Nitrogen fixation
Oxygenation
Photoelectrocatalysis
Solar fuel

ABSTRACT

Solar-driven N₂ fixation offers a green alternative to the highly energy-intensive Haber-Bosch process that releases more than 300 million metric tons of CO₂ annually to form NH₃. However, N₂-reducing photoelectrochemical (PEC) studies have not elucidated how an oxidation reaction affects the N₂ reduction reaction (NRR). Here, we report a bias-free PEC platform for N₂ reduction to NH₃ and H₂O oxidation to O₂ and H₂O₂. Under solar light, the molybdenum-doped bismuth vanadate-based photoanodes extract electrons from H₂O and transfer them to the silicon photovoltaic-wired hematite photocathode. The light-absorbing cathode receives the electrons to drive the NRR, which is influenced by the H₂O oxidation reaction's conditions. Furthermore, the integration of PEC NRR with H₂O₂-dependent biocatalytic oxyfunctionalization achieves simultaneous synthesis of valuable chemicals on both electrodes. This work presents the first example of a PEC NRR platform coupled with H₂O oxidation and H₂O₂-dependent oxygenation for unbiased chemical synthesis using N₂, H₂O, and sunlight.

1. Introduction

Ammonia (NH₃) serves as a fertilizer and an alternative carrier of hydrogen energy [1]. Currently, industrial production of NH₃ relies on the conventional Haber-Bosch process that entails the reaction between N₂ and H₂ using iron-based catalysts [1]. However, the process suffers from consuming over 1% of the global energy production because it operates at high temperature (300–500°C) and pressure (200–300 atm) to dissociate the inert N≡N bond [2,3]. In addition, the reductant H₂ is produced through steam reforming of natural gas, which emits over 300 million metric tons of CO₂ per year, accounting for approximately 1.4% of global CO₂ emissions [1,3].

As an alternative to the energy-intensive and environmentally unfriendly process, aqueous redox chemistry for N₂ reduction to NH₃ has garnered high interest because of (i) better energy efficiency than the Haber-Bosch process by about 20% [4], (ii) no requirement of fossil fuels (and the consequent eradication of CO₂ emission) [5], and (iii) ambient reaction conditions [6]. The N₂ reduction reaction (NRR) requires electrons that are provided by external power source (e.g., potentiostat

[1,3] or sacrificial electron donor (e.g., methanol [7] or ascorbate [8]). For example, recently reported N₂-reductive photoelectrochemical (PEC) systems [9,10] use electrical energy [e.g., −0.1 to −0.2 V vs. the reversible hydrogen electrode (RHE)] in a three-electrode configuration. We envision that the need for electrical energy and artificial electron donors can be eliminated by solar-driven extraction of electrons from H₂O, which functions as an abundant electron donor and a biocompatible solvent [11–13].

Here, we report the first example of unbiased N₂ reduction to NH₃ fueled by H₂O (2N₂ + 6H₂O + sunlight → 4NH₃ + 3O₂) in a two-electrode configuration. As illustrated in Fig. 1, the N₂-reductive PEC system consists of two components: (i) a ferric oxyhydroxide-coated, molybdenum-doped bismuth vanadate (FeOOH/Mo:BiVO₄) photoanode that extracts electrons from H₂O and (ii) a Si photovoltaic (Si PV)-wired hematite (Si/α-Fe₂O₃) photocathode that supplies a large photovoltage (V_{ph}) for bias-free redox reactions, receives the electrons from the photoanode, and achieves the six-electron reduction of N₂ to NH₃ at the surface of α-Fe₂O₃ nanorods. Furthermore, we designed a bias-free combination of NRR with H₂O₂ production driven by two-electron

* Corresponding author.

E-mail address: parkcb@kaist.ac.kr (C.B. Park).

¹ These authors contributed equally to this work.

WOR ($\text{N}_2 + 6\text{H}_2\text{O} + \text{sunlight} \rightarrow 2\text{NH}_3 + 3\text{H}_2\text{O}_2$) (Fig. 1). The in situ generated H_2O_2 activates H_2O_2 -dependent peroxygenases for enantioselective oxyfunctionalization of inert C-H bonds. This peroxygenase-catalyzed hydroxylation converts simple organic compounds into value-added building blocks used in the synthesis of fine chemicals and pharmaceutical intermediates [14,15].

2. Experimental section

2.1. Materials

Iron nitrate nonahydrate, sodium sulfate, ammonium chloride, ammonium- ^{15}N chloride, salicylic acid, sodium citrate tribasic dihydrate, sodium hypochlorite, sodium nitroferrocyanide, hydrazine hydrate, 4-(dimethylamino)benzaldehyde, sodium chloride, potassium chloride, bismuth nitrate pentahydrate, potassium iodide, vanadyl acetylacetonate, dimethyl sulfoxide, *p*-benzoquinone, bis(acetylacetonato) dioxomolybdenum, iron sulfate heptahydrate, horseradish peroxidase, and 2,2'-azino-bis(3-ethylbenzothiazoline-6-sulfonic acid) were purchased from Sigma Aldrich (St. Louis, MO, USA). All chemicals were used without further purification. We used type 1 ultrapure water (18 M Ω cm) from a Direct-Q® 5 UV ultrapure water purification system (Millipore Corp., USA). We prepared a recombinant, evolved peroxygenase from *Agrocyste aegerita* (rAaeUPO) according to the literature [12].

2.2. Synthesis of photocathodes

We slightly modified a reported synthetic method [16] to prepare a hematite electrode via hydrothermal method and high-temperature annealing. A commercial carbon cloth was purchased and washed with acetone, ethanol, and deionized water. For deposition of a β -FeOOH film on the carbon cloth, we first prepared an aqueous solution containing 0.06 M $\text{Fe}(\text{NO}_3)_3 \cdot 9\text{H}_2\text{O}$ and 0.06 M Na_2SO_4 . Then, we sealed the carbon cloth and the clear solution in a Teflon-lined stainless steel autoclave, which was heated in a furnace (Fisher Scientific Co., USA) at 120 °C for 6 h. To transform β -FeOOH into α - Fe_2O_3 , we annealed the β -FeOOH electrode under N_2 flow at 400 °C for 4 h with a heating rate of 1.5 °C min $^{-1}$. To prepare a Si/ α - Fe_2O_3 photocathode, we wired the

as-synthesized α - Fe_2O_3 cathode to a commercial Si photovoltaic (Si PV). The electron-collecting contact area of the Si PV was wired to the α - Fe_2O_3 electrode. The Si PV's hole-collecting contact area was wired to the F:SnO $_2$ (FTO) side of the photoanode using Cu tape.

2.3. Photoelectrochemical N_2 reduction and ammonia quantification

We performed PEC NRR in a three-electrode configuration consisting of a working electrode, a reference electrode (Ag/AgCl, 3 M NaCl), and a counter electrode (carbon cloth). We purged 0.1 M Na_2SO_4 electrolyte with the high-purity N_2 gas (purity: 99.999%) before and during PEC reactions. All potentials were quoted versus the reversible hydrogen electrode (RHE) according to Eq. 1:

$$E_{\text{RHE}} (\text{V}) = E_{\text{Ag/AgCl}} (\text{V}) + 0.209 + 0.059 \times \text{pH} \quad (1)$$

We quantified ammonia using the indophenol blue method with some modifications [1]. We collected 1 mL of a reaction solution, which was mixed with NaOH solution (1 mL, 1 M) containing salicylic acid (5 wt%) and sodium citrate (5 wt%), NaClO solution (0.5 mL, 0.05 M), and sodium nitroferrocyanide solution (0.1 mL, 1 wt%). After stirring for 2 h in dark, we used an ultraviolet-visible (UV-Vis) spectrophotometer (JASCO Inc., Japan) to obtain the absorption spectrum of the mixture solution at 655 nm. The NH_3 production rate and Faradaic efficiency were calculated using Eqs. 2 and 3:

$$\text{Production rate} (\mu\text{g h}^{-1} \text{ cm}^{-2}) = \frac{c_{\text{NH}_3} \times V}{t \times A} \quad (2)$$

$$\text{Faradaic efficiency} (\%) = \frac{3 \times F \times c_{\text{NH}_3} \times V}{17 \times Q} \times 100 \quad (3)$$

where c_{NH_3} is the NH_3 concentration ($\mu\text{g mL}^{-1}$), V is the volume of the electrolyte (mL), t is the reaction time (h), A is the geometrical surface area of the electrode (cm^2), F is the Faraday constant (96,485 C mol $^{-1}$), and Q is the total charge consumed during photoelectrocatalysis. The solar-to-ammonia (STA) conversion efficiency was estimated in a two-electrode configuration according to the Eq. 4:

$$\text{STA} (\%) = \frac{r \times \Delta G}{I \times A} \times 100 \quad (4)$$

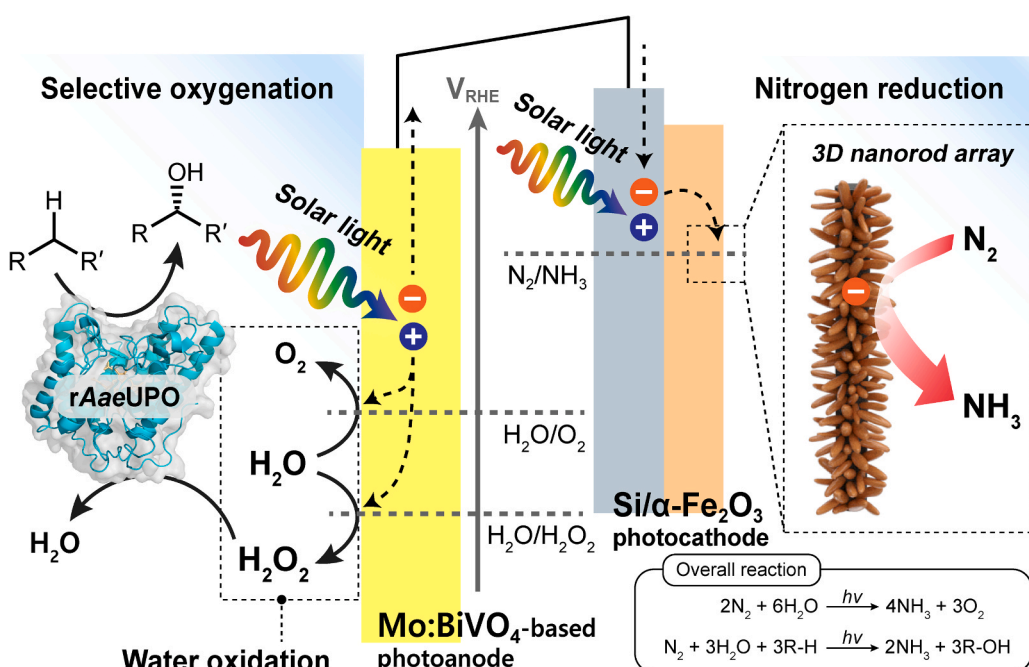


Fig. 1. Schematic illustration of unbiased pairing of N_2 reduction with H_2O oxidation and enantioselective enzymatic synthesis. A Si-wired hematite (Si/ α - Fe_2O_3) photocathode reduces N_2 to NH_3 while a water-oxidizing Mo:BiVO $_4$ -based photoanode extracts electrons from H_2O as an electron donor. The Si/ α - Fe_2O_3 is electrically connected with a Mo:BiVO $_4$ for producing NH_3 and H_2O_2 at cathodic and anodic sites, respectively. The in situ generated H_2O_2 activates rAaeUPO for enantioselective oxyfunctionalization reactions.

where r is the NH_3 production rate (mmol s^{-1}), ΔG is the Gibbs free energy of overall NRR (330 kJ mol^{-1}), and I is the light density (100 mW cm^{-2}). For H_2 quantification, we used a micro gas chromatograph (Micro GC fusion, INFICON Inc., USA) that was equipped with a micro thermal conductivity detector and a Molsieve 5 A column.

2.4. Hydrazine quantification

We quantified N_2H_4 using Watt and Chrisp method [1]. We prepared a coloring solution by dissolving 0.6 g of $p\text{-C}_9\text{H}_{11}\text{NO}$ in a mixture solution of 30 mL absolute ethanol and 3 mL concentrated HCl. Typically, 0.5 mL of a reaction solution was mixed with 0.5 mL of the coloring solution. After stirring for 10 min in dark, the UV-Vis spectra of the mixture solution were acquired at 455 nm.

2.5. Nuclear magnetic resonance spectroscopic analysis

We recorded ^1H nuclear magnetic resonance (^1H NMR) spectra using a Bruker AVANCE NEO 500 MHz to detect NH_3 . After PEC reduction of $^{14}\text{N}_2$, a reaction solution was collected and acidified with 0.5 M H_2SO_4 . Subsequently, we mixed the acidified reaction solution with $[\text{D}_6]\text{dimethylsulfoxide}$ ($[\text{D}_6]\text{DMSO}$) and a maleic acid as a solvent and an internal standard, respectively. We used zgpg30 as the NMR pulse sequence with 128 and 2048 scans for qualitative and quantitative analyses, respectively. When we isotope labeling experiment, we used $^{15}\text{N}_2$ gas (Sigma-Aldrich, 98 atom % ^{15}N) as a feeding gas and set the NMR scan number to 1024.

2.6. Preparation of photoanodes

We rinsed a commercial FTO glass with KOH solution, deionized water, and ethanol. We prepared a precursor solution by dissolving Bi (NO_3) $_3 \cdot 5\text{H}_2\text{O}$ (0.04 M), HNO_3 ($2 \mu\text{L mL}^{-1}$), and KI (0.4 M) in deionized water (25 mL) and then adding 10 mL of absolute ethanol containing $p\text{-benzoquinone}$ (0.23 M). The FTO substrate was immersed in the precursor solution, and the cathodic bias of -0.1 V (vs. Ag/AgCl) was applied for 3 min using a potentiostat/galvanostat (WMPG 1000, WonATech Co., Korea). For transformation of BiOI into $\text{Mo}:\text{BiVO}_4$, we uniformly dropped a DMSO solution—containing $\text{VO}(\text{acac})_2$ (0.2 M) and $\text{MoO}_2(\text{acac})_2$ (2 mM)—on the BiOI electrode and heated in a Lindberg/Blue M muffle furnace (Fisher Scientific Corp., USA) at 450°C for 2 h with a heating rate of 1°C min^{-1} . After the thermal treatment, we immersed the sample in a 1 M NaOH solution with gentle stirring to eliminate unwanted V_2O_5 crusts. For photo-assisted electrodeposition of FeOOH adlayer on the $\text{Mo}:\text{BiVO}_4$ electrode, we dissolved 0.1 M $\text{FeSO}_4 \cdot 7\text{H}_2\text{O}$ in N_2 -enriched deionized water and immersed the $\text{Mo}:\text{BiVO}_4$ in the solution. Then, we applied 0.25 V (vs. Ag/AgCl) to a $\text{Mo}:\text{BiVO}_4$ electrode under irradiation (2 mW cm^{-2}) for 20 min.

2.7. Photoelectrochemical analysis of photoanodes

We adopted a three-electrode configuration consisting of Ag/AgCl (3 M NaCl) as a reference electrode and Pt wire as a counter electrode. We used phosphate-buffered saline (PBS) (10 mM, pH 7.0) as an anolyte solution. We conducted linear sweep voltammetric and chronoamperometric analyses using a potentiostat/galvanostat (WMPG 1000, WonATech Co., Korea). We used an impedance analyzer (ZIVE SP1, WonATech Co., Korea) to acquire Nyquist plots at a frequency of 100 kHz to 0.1 Hz and an AC potential amplitude of 25 mV. We used a xenon lamp as a light source.

2.8. Material characterization

The morphologies of electrodes were investigated using an SU8230 field emission scanning microscope (SEM; Hitachi Co., Japan) and a transmission electron microscope (TEM; Talos F200X, FEI Company,

USA). X-ray photoelectron spectroscopy (XPS; Thermo VG Scientific, UK) was used to confirm the elemental components of electrodes. The crystal structures of electrodes were examined using X-ray diffractometer (XRD; RIGAKU Co. Japan) with a $\text{Cu K}\alpha$ radiation wavelength of 1.5418 \AA . UV-Vis absorption and transmittance spectra of photoelectrodes were obtained using UV-Vis spectrophotometer (Perkin Elmer, USA). Photoluminescence spectra were recorded by a spectrofluorometer (RF-6000, SHIMADZU Co., Inc., Japan).

2.9. H_2O_2 quantification

We used 2,2'-azino-bis(3-ethylbenzothiazoline-6-sulfonic acid) (ABTS) assay to quantify H_2O_2 . After driving $\text{Mo}:\text{BiVO}_4$ -driven photoanodic reactions, we collected a reaction solution and mixed it with a colorimetric reagent [potassium phosphate solution (100 mM, pH 5.0) containing 2.5 U horseradish peroxidase and 2 mM ABTS]. After incubated at room temperature for 10 min, the absorbance of the mixture was monitored using the UV-Vis spectrophotometer at 420 nm.

2.10. Bias-free photoelectrocatalytic N_2 reduction coupled with H_2O oxidation and biocatalytic oxyfunctionalization reactions

We coupled NRR with H_2O oxidation reaction in a two-compartment configuration, which was connected by a salt bridge. The light source was a 450 W xenon-arc lamp (Newport Co., USA). We immersed a $\alpha\text{-Fe}_2\text{O}_3$ cathode in 0.1 M Na_2SO_4 electrolyte (pH 7.0) and a $\text{FeOOH}/\text{Mo}:\text{BiVO}_4$ photoanode in a PBS solution (10 mM, pH 7.0). The Si PV was placed in front of a cathodic cell, and connected to the $\alpha\text{-Fe}_2\text{O}_3$ cathode. The geometrical surface areas of $\text{FeOOH}/\text{Mo}:\text{BiVO}_4$, $\alpha\text{-Fe}_2\text{O}_3$, and Si PV were 1, 1, and 6 cm^2 , respectively. For coupling of PEC NRR with photobiocatalytic reaction, we substituted $\text{FeOOH}/\text{Mo}:\text{BiVO}_4$ with $\text{Mo}:\text{BiVO}_4$. We prepared an anodic chamber with the PBS solution (10 mM, pH 7) containing 20 nM rAaeUPO and a substrate. After the photoenzymatic reactions, we quantified enzymatic products by a 7890 A gas chromatograph (Agilent Technologies Inc., USA) equipped with a CP-Chirasil-Dex CB column (25 m, 0.32 mm, $0.25 \mu\text{m}$) [12]. We extracted an enzymatic product from a reaction sample using ethyl acetate (containing 5 mM 1-octanol as the internal standard), and dried it over MgSO_4 . The detailed oven-temperature programs were tabulated in Table S1. The enantiomeric excess (e.e.), total turnover number (TTN), and turnover frequency (TOF) of rAaeUPO were calculated according to the Eqs. 3, 4, and 5 as follows:

$$\text{e.e.}(\%) = \frac{|\text{Mole of an enantiomer} - \text{Mole of the other enantiomer}|}{\text{Total moles of products}} \times 100 \quad (3)$$

$$\text{TTN}_{\text{rAaeUPO}} = \frac{\text{Maximum concentration of product}}{\text{Concentration of rAaeUPO}} \quad (4)$$

$$\text{TOF}_{\text{rAaeUPO}}(\text{h}^{-1}) = \frac{\text{Turnover number of rAaeUPO}}{\text{Time}} \quad (5)$$

3. Results

3.1. $\text{Si}/\alpha\text{-Fe}_2\text{O}_3$ photocathode for N_2 fixation

We synthesized a $\text{Si}/\alpha\text{-Fe}_2\text{O}_3$ photocathode by (i) the formation of $\beta\text{-FeOOH}$ layer on a carbon cloth, (ii) the thermal phase transformation from $\beta\text{-FeOOH}$ to $\alpha\text{-Fe}_2\text{O}_3$ under N_2 -rich conditions (purity: 99.999 %), and (iii) electrical wiring $\alpha\text{-Fe}_2\text{O}_3$ with a Si PV in a series. As shown in the plan-view scanning electron microscopic image (Fig. 2a), the synthesized $\alpha\text{-Fe}_2\text{O}_3$ exhibited a three-dimensional nanostructure consisting of nanorods (diameter: $\sim 50 \text{ nm}$). We verified that the nanostructured ferric oxide exhibited the $\alpha\text{-Fe}_2\text{O}_3$ phase using X-ray diffraction analysis (Fig. 2b). Next, we performed X-ray photoelectron spectroscopy (XPS) on the $\alpha\text{-Fe}_2\text{O}_3$ electrocatalyst, and verified that it

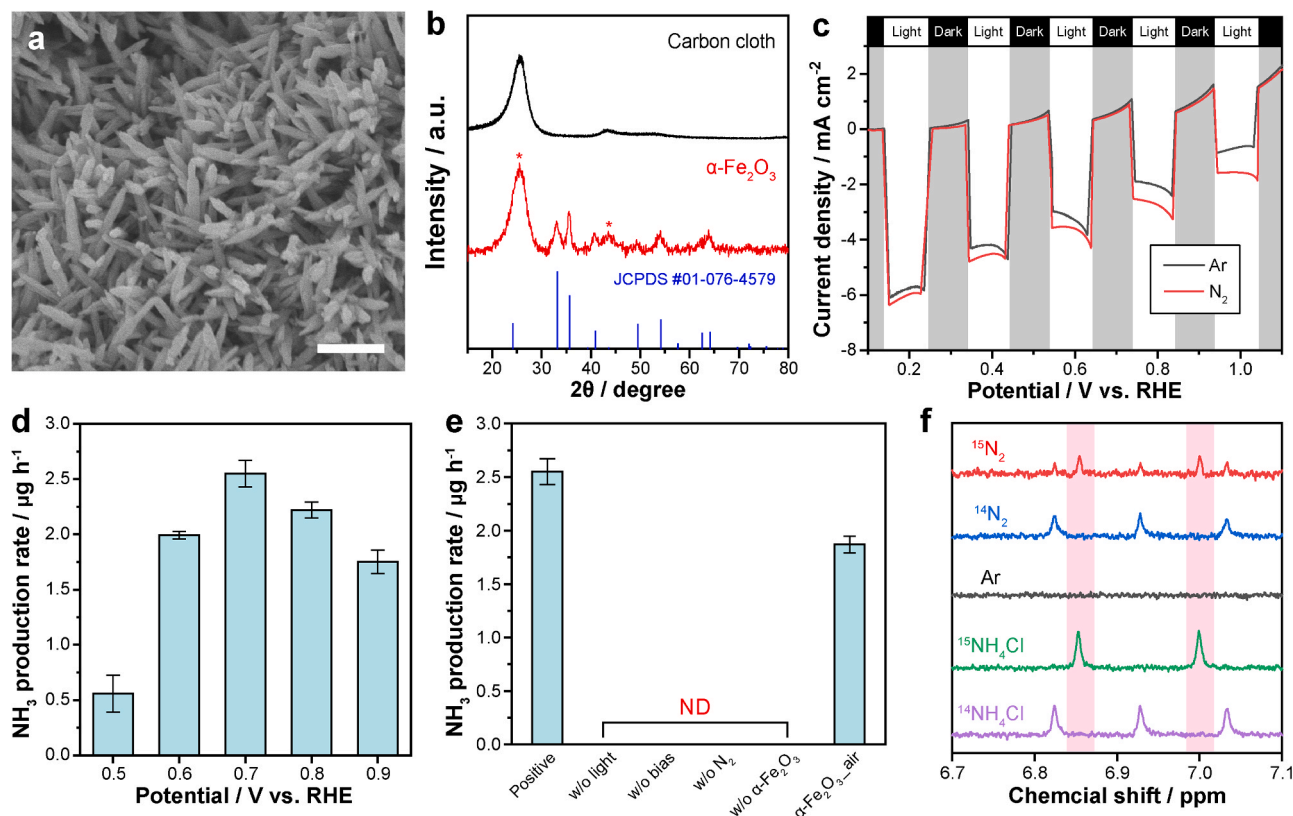


Fig. 2. Photoelectrochemical N₂-to-NH₃ conversion using Si/α-Fe₂O₃ photocathode. (a) Plan-view SEM image of α-Fe₂O₃. Scale bar: 500 nm. (b) XRD patterns of carbon cloth and α-Fe₂O₃. The diffraction file number of α-Fe₂O₃ is #01-076-4579, which is provided by the joint committee on powder diffraction standards-international center for diffraction data. Asterisks denote the XRD peaks of carbon cloth. (c) Chopped linear sweep voltammograms of Si/α-Fe₂O₃ under Ar- or N₂-enriched environments. Scan rate: 20 mV s⁻¹. Electrolyte: 0.1 M Na₂SO₄ aqueous solution. (d) NH₃ production rates of the Si/α-Fe₂O₃ photocathode at different applied potentials. (e) A series of control experiments for PEC NRR by Si/α-Fe₂O₃. Potential: 0.7 V (vs. RHE). (f) ¹H NMR spectra of PEC NRR experiments. Feed gas: ¹⁵N₂ or ¹⁴N₂. Geometrical surface area of the photocathode in (c-f): 1 cm². Reaction time in (d-f): 2 h. Light intensity in (c-f): 1 sun (air mass 1.5 global, 100 mW cm⁻²). Electrolyte volume in (c-f): 30 mL. Error bars correspond to the standard deviation ($n = 3$). ND: not detected.

contained Fe and O atoms in the Fe³⁺ and O²⁻ states, respectively (Fig. S1). Under 1-sun irradiation (air mass 1.5 global, 100 mW cm⁻²), the J - V plot of Si/α-Fe₂O₃ was anodically shifted by 1.25 V than that of α-Fe₂O₃ (Fig. S2), which we attribute to the Si PV's V_{ph} . It indicates that Si/α-Fe₂O₃ photocathode requires a less cathodic bias than α-Fe₂O₃ cathode under solar light.

We demonstrated the capability of Si/α-Fe₂O₃ photocathode to convert N₂ into NH₃ in a three-electrode configuration under 1-sun illumination. According to our chopped linear sweep voltammograms (Fig. 2c), the Si/α-Fe₂O₃ produced an anodic current density in N₂-enriched 0.1 M Na₂SO₄ solution under dark conditions, indicating imperceptible NRR reactions. In stark contrast, the photocathode generated much higher photocathodic current density under N₂-rich conditions than Ar-rich conditions (Fig. 2c), signifying the transfer of photoexcited electrons to N₂ molecules. Controlled potential photoelectrolysis (CPPE) demonstrated NH₃ production from 0.5 to 0.9 V (vs. the reversible hydrogen electrode, RHE) (Fig. 2d). We quantified NH₃ using the indophenol blue method and UV-Vis spectroscopy because UV-Vis and quantitative ¹H nuclear magnetic resonance (NMR) tools provide no significantly different concentrations of NH₃ in statistics (see Fig. S3 for details). The highest average NH₃ production rate and Faradaic efficiency were 2.55 μg h⁻¹ at 0.7 V (vs. RHE) and 10.3% at 0.8 V (vs. RHE), respectively (Figs. 2d and S4). The application of more negative potentials than 0.7 V (vs. RHE) decreased NH₃ production rates. We attribute the result to the competing hydrogen evolution reaction (HER) (Fig. S5) from the proton adsorption on the α-Fe₂O₃ surface [17,18]. Control experiments in the absence of light, electrical bias, N₂, or α-Fe₂O₃ did not produce NH₃ (Fig. 2e), and N₂ feed gas itself did not

contain NH₃ (Fig. S6a). In addition, hydrazine (N₂H₄) was not formed as a side product at 0.7 V (vs. RHE) (Figs. S7 and S8), which highlights the Si/α-Fe₂O₃'s excellent selectivity toward NRR. Furthermore, we confirmed the robust stability of Si/α-Fe₂O₃-driven NRR. As shown in Fig. S9, Si/α-Fe₂O₃ exhibited (i) steady NH₃ production rates along with photocathodic currents and (ii) no change in morphology and crystallographic structure during a five-iteration experiment.

We performed isotope labeling experiments to identify the chemical source of NH₃. According to our ¹H NMR spectroscopy, Si/α-Fe₂O₃ formed ¹⁴NH₄⁺ in a ¹⁴N₂-enriched solution after CPPE (1 sun, 0.7 V vs. RHE, 2 h) (Fig. 2f), and ¹⁴N₂ feed gas did not contain ¹⁴NH₃ (Fig. S6b). The substitution of ¹⁴N₂ with ¹⁵N₂ resulted in the generation of ¹⁵NH₄⁺ (Fig. 2f), which indicates that NH₃ production originated from the PEC NRR, not NO₃⁻ reduction or NH₃ pollution. We also detected ¹⁴N triplet NMR peaks in the isotope experiment, which we attribute to the dissolution of atmospheric ¹⁴N₂ into the ¹⁵N₂-containing electrolyte solution. The control experiment using Ar gas did not show NH₄⁺'s NMR peaks (Fig. 2f), reaffirming the Si/α-Fe₂O₃-driven NRR to NH₃.

The oxygen vacancy (O_v) of a metal oxide (e.g., WO₃ [19], TiO₂ [20, 21], LaFeO₃ [22]) has been reported to function as an active site that accelerates catalytic reactions by, for example, absorbing N₂ molecules, facilitating hydrogenation steps, and/or decreasing the free energy change at a potential-determining step (Table S2). Thus, we investigated the effect of α-Fe₂O₃'s O_v in N₂ fixation to NH₃. We synthesized α-Fe₂O₃ that was annealed in air (namely, α-Fe₂O₃-air) during thermal phase transformation. According to our O 1s XPS analysis (Fig. S10), the substitution of N₂ with air resulted in a lower abundance of O_v by 7%p, which we attribute to the role of O₂ molecules [23] to suppress the

formation of O_V during thermal treatment of metal oxides. We found that NH_3 production rate of the $Si/\alpha-Fe_2O_3$ was 1.37 times higher than that of the $Si/\alpha-Fe_2O_3$ -air photocathode. We speculate that an increase in the concentration of $\alpha-Fe_2O_3$'s O_V may boost N_2 adsorption and/or $N\equiv N$ activation based on literature on density functional theory calculations that elucidate the important role of metal oxides' O_V in accelerating NRR.

3.2. FeOOH/Mo:BiVO₄ photoanode for H₂O oxidation

To extract electrons from H₂O and supply them to the $Si/\alpha-Fe_2O_3$ photocathode, we used Mo:BiVO₄ because of its high stability under aqueous environments and excellent WOR kinetics [24,25]. We synthesized a Mo:BiVO₄ electrode through (i) electrodepositing bismuth oxyiodide (BiOI) film on a fluorine-doped tin oxide and (ii) converting BiOI to Mo:BiVO₄ via thermal and chemical treatments. We further photoelectrochemically deposited FeOOH cocatalyst on the Mo:BiVO₄ photoanode because the adlayer is a highly active catalyst for H₂O oxidation at moderate potentials by suppressing surface charge recombination and minimizing the kinetic barrier [25–28]. We confirmed the formation of amorphous FeOOH layer (thickness: ~5 nm) on the crystalline Mo:BiVO₄ using XPS, TEM, and energy-dispersive X-ray spectroscopic elemental mapping (Figs. S11a, S11b, S11c, and S12). The FeOOH deposition did not change the Mo:BiVO₄'s nanostructured morphology (Fig. S11d), monoclinic scheelite phase (Fig. S11e), light absorption property, and direct bandgap (2.5 eV) (Fig. S11f).

We verified the capability of FeOOH cocatalyst to accelerate Mo:BiVO₄'s WOR. As shown in Fig. 3a and S13a, FeOOH/Mo:BiVO₄ exhibited a cathodic shift of the onset potential for H₂O oxidation (~230 mV), an enhanced photoanodic current from 0.4 to 1.4 V (vs. RHE), and a lower Tafel slope in a phosphate-buffered saline (10 mM, pH 7.0) solution. We attribute the improved WOR performance to (i) a decreased charge-transfer resistance (Figs. S13b and S13c), (ii) increased efficiency of charge transfer at the electrode|electrolyte

interface (Fig. S13d), (iii) reduced charge recombination behavior (Figs. S14a and S14b), and (iv) longer decay time of charge carriers (Figs. S14c and S14d), which we obtained using electrochemical impedance spectroscopy [29], (transient) voltammetric analysis, and photoluminescence spectroscopy [30]. Detailed analytical explanations are shown in the caption of Figs. S13 and S14.

3.3. Solar-driven unbiased N₂ reduction coupled with H₂O oxidation

Having substantiated the NRR and WOR driven by $Si/\alpha-Fe_2O_3$ and FeOOH/Mo:BiVO₄, respectively, we constructed a full PEC structure (i.e., FeOOH/Mo:BiVO₄| $Si/\alpha-Fe_2O_3$) to drive NRR fueled by H₂O as an electron donor. We expected bias-free coupling of NRR and WOR according to the intersection of the overlaying $|J|$ - V plots of FeOOH/Mo:BiVO₄ and $Si/\alpha-Fe_2O_3$ (Fig. 3a). The exposure of the PEC system to solar light triggered NH_3 production with an average rate of $1.476 \mu g h^{-1}$ (Fig. 3b) and a solar-to-ammonia conversion efficiency of 0.0080%. In the absence of light, Si PV, or N_2 molecules, NH_3 formation was imperceptible (Fig. 3b), which highlights the unbiased NRR to NH_3 . When we substituted $\alpha-Fe_2O_3$ with $\alpha-Fe_2O_3$ -air, the NH_3 formation rate decreased by 1.36 times. In addition, the omission of FeOOH on Mo:BiVO₄ decreased the production rate significantly from 1.476 to $0.328 \mu g h^{-1}$ (Fig. 3b), indicating that WOR is responsible for supplying electrons for NRR.

Based on the importance of WOR in NRR, we investigated the role of H₂O as an electron donor for unbiased NRR by FeOOH/Mo:BiVO₄| $Si/\alpha-Fe_2O_3$ system. To control H₂O concentration in a cathodic electrolyte solution, we used an anhydrous dimethyl sulfoxide (DMSO) that is miscible with the aqueous electrolyte. Our chronoamperometric analysis shows that current density increased with increasing volume ratio of H₂O/DMSO under 1-sun illumination, and the current density was negligible under dark conditions (Figs. 3c and S15). In accordance with the result, we obtained a saturation curve that shows the relationship between the rate of NH_3 production and the H₂O/DMSO volume ratio

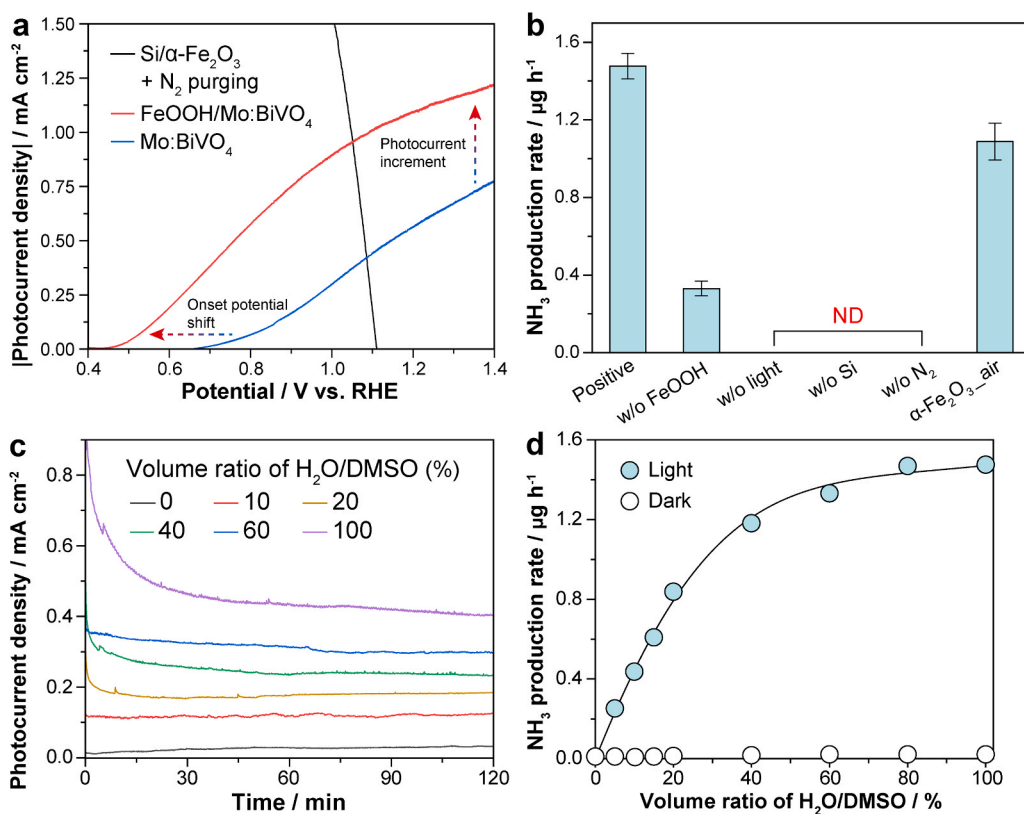


Fig. 3. Unbiased reduction of N_2 to NH_3 by the FeOOH/Mo:BiVO₄| $Si/\alpha-Fe_2O_3$ photoelectrocatalytic system. (a) Overlap of $|J|$ - V profiles of a $Si/\alpha-Fe_2O_3$ photocathode (black) and Mo:BiVO₄-based photoanodes (red and blue). (b) Control experiments for bias-free PEC NRR driven by FeOOH/Mo:BiVO₄| $Si/\alpha-Fe_2O_3$. (c) Chronoamperometric curves with various H₂O/DMSO volume ratios in an anodic compartment. (d) Effect of H₂O/DMSO volume ratios on the rate of NH_3 formation. Light condition in (a-d): 1 sun. Geometrical surface areas of photocathodes and photoanodes in (a-d): 1 cm². Reaction time in (b, d): 2 h. Electrolyte volume in the cathodic compartment: 15 mL. Electrolyte volume in the anodic compartment: 10 mL. Error bars correspond to the standard deviation ($n = 3$). ND: not detected.

(Fig. 3d). We observed that unbiased NH_3 formation kinetics decreased with decreasing volume ratio of H_2O /DMSO, and became imperceptible when the electrolyte solution consisted of DMSO only. The result highlights the transfer of photoexcited electrons from H_2O electron donor to N_2 reactant. In addition, the NH_3 production kinetics linearly increased up to 57% of its maximal production rate until the volume ratio of H_2O /DMSO reached 20%. We ascribe it to the saturation of $\text{FeOOH}/\text{Mo}:\text{BiVO}_4$'s active sites for WOR.

Furthermore, we explored the effect of photoexcited electrons and holes on the NRR. We added sodium sulfite (Na_2SO_3) and sodium persulfate ($\text{Na}_2\text{S}_2\text{O}_8$) as a hole and electron scavenger, respectively. As shown in Fig. S16a, the addition of Na_2SO_3 to an anolyte decreased the NH_3 production rate. Although Na_2SO_3 increased the operating current of $\text{FeOOH}/\text{Mo}:\text{BiVO}_4|\text{Si}/\alpha\text{-Fe}_2\text{O}_3$ (Fig. S16b), it shifted $\text{Si}/\alpha\text{-Fe}_2\text{O}_3$'s potential anodically in $\text{FeOOH}/\text{Mo}:\text{BiVO}_4|\text{Si}/\alpha\text{-Fe}_2\text{O}_3$ architecture (Fig. S16c), and consequently decreased NH_3 production on $\text{Si}/\alpha\text{-Fe}_2\text{O}_3$ (Fig. S16c). In contrast, supplementing $\text{Na}_2\text{S}_2\text{O}_8$ to a catholyte resulted in no production of NH_3 (Fig. S16a). It highlights that $\text{Si}/\alpha\text{-Fe}_2\text{O}_3$'s photoexcited electrons participate in NRR. Consistent with this result, $\text{Si}/\alpha\text{-Fe}_2\text{O}_3$ did not generate NH_3 when we added Na_2SO_3 and $\text{Na}_2\text{S}_2\text{O}_8$ into the anolyte and catholyte, respectively, at the same time (Fig. S16a).

3.4. Photobiocatalytic oxyfunctionalization coupled with N_2 reduction

Oxidoreductases catalyze various synthetically useful reactions with exceptional selectivity and environmental benignity [31–40], which solid-state catalytic electrodes cannot achieve. In this study, we

attempted to pair NRR with oxidoreductase-driven oxygenation of inert C-H bonds (Fig. 1). As a model biocatalyst, we employed the recombinant, evolved unspecific peroxygenase from *Agrocybe aegerita* (rAaeUPO) [12,13,41–43]. Considering that rAaeUPO requires H_2O_2 as a sole oxidant [41,44,45], we did not deposit FeOOH adlayer on the $\text{Mo}:\text{BiVO}_4$ photoanode. This is because FeOOH 's Fermi level is more negative [46] than the redox potential [12] of two-electron WOR ($2\text{H}_2\text{O} + 2\text{h}^+ \rightarrow \text{H}_2\text{O}_2 + 2\text{H}^+$) (Fig. S17a). We confirmed that photoelectroactivated $\text{Mo}:\text{BiVO}_4$ gradually formed H_2O_2 , whereas $\text{FeOOH}/\text{Mo}:\text{BiVO}_4$ formed a negligible amount of H_2O_2 (Fig. S17b).

Although $\text{Mo}:\text{BiVO}_4$ generates more H_2O_2 than $\text{FeOOH}/\text{Mo}:\text{BiVO}_4$, the target redox reaction [$\text{N}_2(\text{g}) + 6\text{H}_2\text{O}(\text{l}) \rightarrow 2\text{NH}_3(\text{aq}) + 3\text{H}_2\text{O}_2(\text{aq})$] is rather sluggish in the $\text{Mo}:\text{BiVO}_4|\text{Si}/\alpha\text{-Fe}_2\text{O}_3$ system. We ascribe this to $\text{Mo}:\text{BiVO}_4$'s slow electron extraction from H_2O , which results in a lower photocurrent density (Fig. 3a). To accelerate the redox reaction, we applied external electrical bias and found that ~ 0.5 V bias is required to optimize NH_3 production rate (Fig. S18). Based on this result, we replaced the original Si PV ($V_{\text{ph}} = 1.25$ V) with another Si PV having a higher V_{ph} of 1.80 V to realize bias-free coupling of NH_3 and H_2O_2 production. The theoretical and actual operation currents of $\text{Mo}:\text{BiVO}_4|\text{Si}(1.80\text{ V})/\alpha\text{-Fe}_2\text{O}_3$ were approximately 2.3 times higher than those of $\text{Mo}:\text{BiVO}_4|\text{Si}(1.25\text{ V})/\alpha\text{-Fe}_2\text{O}_3$ (Fig. S19).

Building on the results, we explored unbiased pairing of NH_3 production with enantioselective oxyfunctionalization using $\text{Mo}:\text{BiVO}_4|\text{Si}(1.80\text{ V})/\alpha\text{-Fe}_2\text{O}_3$ (Fig. 1). We analyzed the product using gas chromatography-mass spectrometry (GC-MS) and GC (Figs. S20a and S21a). As shown in Fig. 4a, ethylbenzene was hydroxylated to enantiopure (*R*)-1-phenylethanol [$> 99\%$ enantiomeric excess (e.e.)] with a

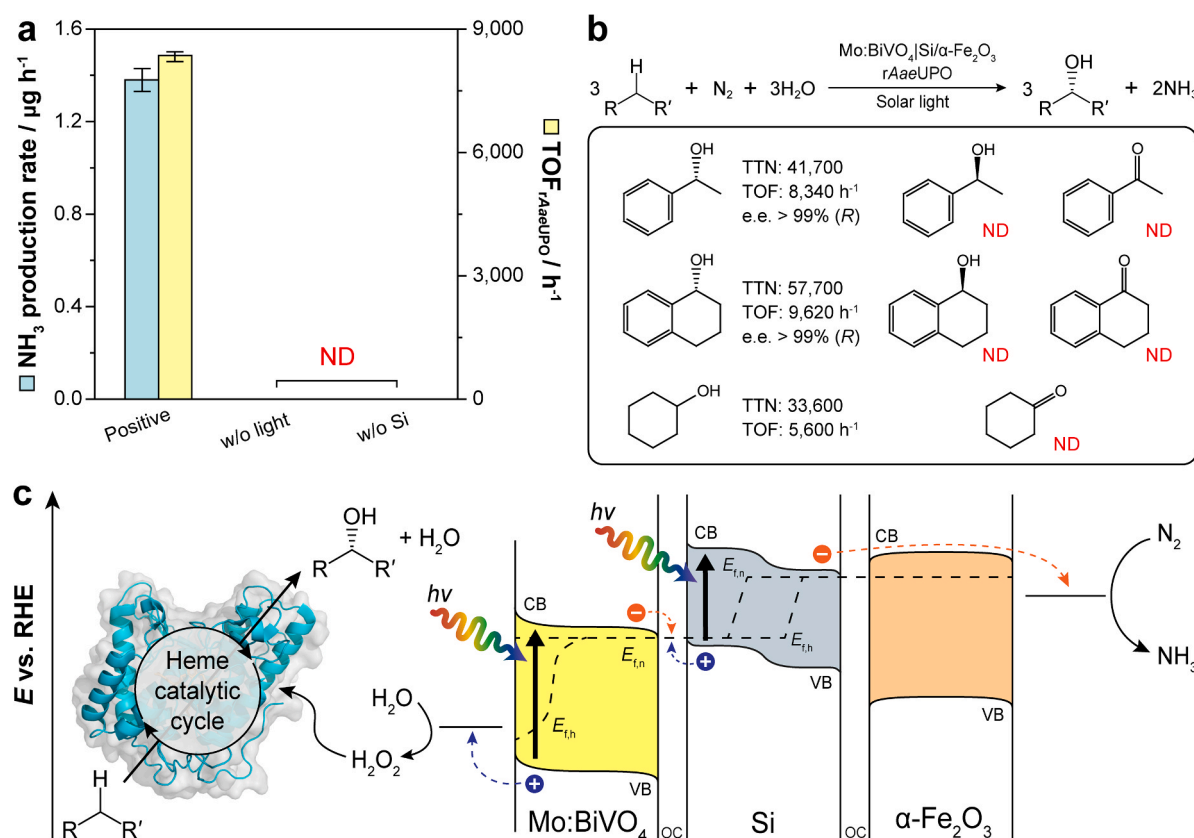


Fig. 4. Enantioselective photobiocatalytic oxyfunctionalization coupled with N_2 reduction. (a) Control experiments of bias-free biocatalytic hydroxylation paired with N_2 reduction. (b) Other rAaeUPO-driven oxygenation reactions driven by $\text{Mo}:\text{BiVO}_4|\text{Si}/\alpha\text{-Fe}_2\text{O}_3$. (c) Plausible mechanism of unbiased combination of N_2 reduction and UPO biocatalysis. OC: ohmic contact. CB: conduction band. VB: valence band. $E_{f,n}$: quasi-Fermi level of electrons. $E_{f,h}$: quasi-Fermi level of holes. Catholyte in (a, b): Na_2SO_4 solution (0.1 M, 15 mL). Anolyte in (a, b): phosphate-buffered saline (10 mM, pH 7.0, 10 mL) containing rAaeUPO and substrate. Geometrical surface areas of photocathodes and photoanodes in (a, b): 1 cm^2 . Reaction time in (b): 6 h. Light intensity in (a, b): 1 sun. Error bars correspond to the standard deviation ($n = 3$). ND: not detected.

turnover frequency for $rAaeUPO$ ($TOF_{rAaeUPO}$) of 8340 h^{-1} and a total turnover number of $rAaeUPO$ ($TTN_{rAaeUPO}$) of 41,700 in the anodic site, while N_2 was reduced to NH_3 at the rate of $1.38 \mu\text{g h}^{-1}$ in the cathodic site. Note that (R)-1-phenylethanol was not further oxidized to acetophenone (Fig. 4b), which indicates the high selectivity in enantioselective hydroxylation. The molar ratio of NH_3 to (R)-1-phenylethanol was estimated to be 1:16 (Fig. S22), which is different from the molar ratio (2:3) for coupling of NRR and $rAaeUPO$ catalysis ($N_2 + 3R-H + 3H_2O \rightarrow 2NH_3 + 3R-OH$). We attribute it to another possible oxidation-reduction coupling, such as H_2 evolution and enzymatic oxyfunctionalization ($R-H + H_2O \rightarrow R-OH + H_2$) (Fig. S5). Furthermore, the $Mo:BiVO_4|Si(1.80 \text{ V})/\alpha-Fe_2O_3$ platform was applied to other oxyfunctionalization reactions such as enantioselective hydroxylation of tetralin ($TOF_{rAaeUPO} = 9620 \text{ h}^{-1}$, $TTN_{rAaeUPO} = 57,700$, e.e. > 99%) and cyclohexane ($TOF_{rAaeUPO} = 5600 \text{ h}^{-1}$, $TTN_{rAaeUPO} = 33,600$) (Figs. 4b, S20, and S21). All of the unbiased enzymatic reactions required light, Si PV, $rAaeUPO$, and substrate (Figs. 4a and S23).

Based on the widely accepted PEC mechanism [16,25,47–50], we propose a bias-free pathway of integrating NRR with $rAaeUPO$ -mediated oxygenation reactions (Fig. 4c). Both photoelectrodes (i.e., $Mo:BiVO_4$ and Si) absorb solar light to generate photoexcited electrons and holes with the corresponding quasi-Fermi levels of electrons ($E_{f,n}$) and holes ($E_{f,h}$), respectively. Because $E_{f,h}$ is more positive than the redox potential of two-electron H_2O oxidation, the $Mo:BiVO_4$ photoanode transfers its photoexcited holes to H_2O and produces H_2O_2 . Subsequently, $rAaeUPO$ consumes H_2O_2 and generates the catalytically active oxoferryl heme that catalyzes enantioselective oxygenation [12]. The photoexcited electrons of the $Mo:BiVO_4$ are recombined with the Si PV's photoexcited holes, whereas Si PV's photoexcited electrons are delivered to the $\alpha-Fe_2O_3$'s conduction band. The excited electrons then participate in N_2 -to- NH_3 conversion at the surface of $\alpha-Fe_2O_3$ because $E_{f,n}$ is more negative than the redox potential of six-electron reduction of N_2 . In terms of voltage, $Mo:BiVO_4$ photoelectrode and Si PV harvests solar light to generate a V_{ph} ($= |E_{f,n} - E_{f,h}|$) of approximately 1.45 V (Fig. S24) and 1.80 V, respectively. The total V_{ph} ($\sim 3.25 \text{ V}$) is larger than the thermodynamic voltage and overpotentials for integrating N_2 fixation with H_2O oxidation, enabling the unbiased target reaction.

4. Discussion

The PEC NRR system has emerged as a promising platform to convert N_2 into NH_3 , which combines the advantages of electrocatalytic and photocatalytic processes. This approach harvests clean solar energy to generate photoexcited charge carriers and applies an electrical bias to

increase the redox abilities of the charge carriers. In this sense, the majority of PEC systems [9,10,51,52] have focused on developing NRR half-reaction in a three-electrode configuration, which must need an electrical potential between a working electrode and a reference electrode. In addition, the three-electrode configuration requires a counter electrode to balance the current of the working electrode, which indicates that an anodic reaction at the counter electrode is not the concern of the previous PEC NRR studies [53].

Moving beyond the conventional approach, we established the unbiased photoelectrocatalytic pairing of NRR with WOR or biocatalytic synthesis in two-electrode configuration, which converts N_2 and H_2O to value-added chemicals (e.g., NH_3 , enantiopure alcohols). This simultaneous NRR and enzymatic oxygenation occurs at individual half-reaction sites. The $Mo:BiVO_4$ -based photoanodes exhibit a relatively small bandgap (2.5 eV) and a positive quasi-Fermi level of holes [46], which is advantageous for solar-driven WOR. The photoactivated Si PV makes electrons' potential more negative to facilitate NRR on the $\alpha-Fe_2O_3$ catalyst. We assembled these photoelectrocatalysts to construct a full PEC system that converts solar light, N_2 , and H_2O to valuable compounds without external electrical bias. The PEC system compares favorably with a state-of-the-art PEC platform [24] that anodically activates $rAaeUPO$ (Fig. 5). The reported PEC cell drove $rAaeUPO$ catalysis ($TTN_{rAaeUPO} = 10,000$, $TOF_{rAaeUPO} = 5000 \text{ h}^{-1}$) at 0.8 V. The $TTN_{rAaeUPO}$ and $TOF_{rAaeUPO}$ of the $Mo:BiVO_4|Si/\alpha-Fe_2O_3$ assembly were higher even under bias-free conditions. Follow-up studies are needed to improve NH_3 production rate through, for example, (i) elucidating the detailed mechanism of O_v using computational quantum mechanical modeling methods, (ii) controlling O_v densities to increase the active site for NRR, and (iii) constructing a hydrophobic support on the $\alpha-Fe_2O_3$ to suppress HER. In addition, modification of surface morphology of $Mo:BiVO_4$ -based photoanodes would increase hole concentrations at the photoanode|electrolyte interface [54], which accelerates the photoanodic performance of electron extraction from H_2O . These studies will broaden the scope of the platform to other redox reactions (e.g., lignin valorization, alcohol oxidation, enzymatic dehydrogenation) [41,55] with enhanced productivities.

5. Conclusion

We report bias-free pairing of NRR with WOR and UPO biocatalysis in a two-electrode configuration using Si/ $\alpha-Fe_2O_3$ photocathode and $Mo:BiVO_4$ -based photoanode. The photocathodic half-reaction occurred via (i) transfer of photoexcited electrons from Si to $\alpha-Fe_2O_3$ and (ii) electrocatalytic reduction of N_2 to NH_3 at the surface of $\alpha-Fe_2O_3$. To

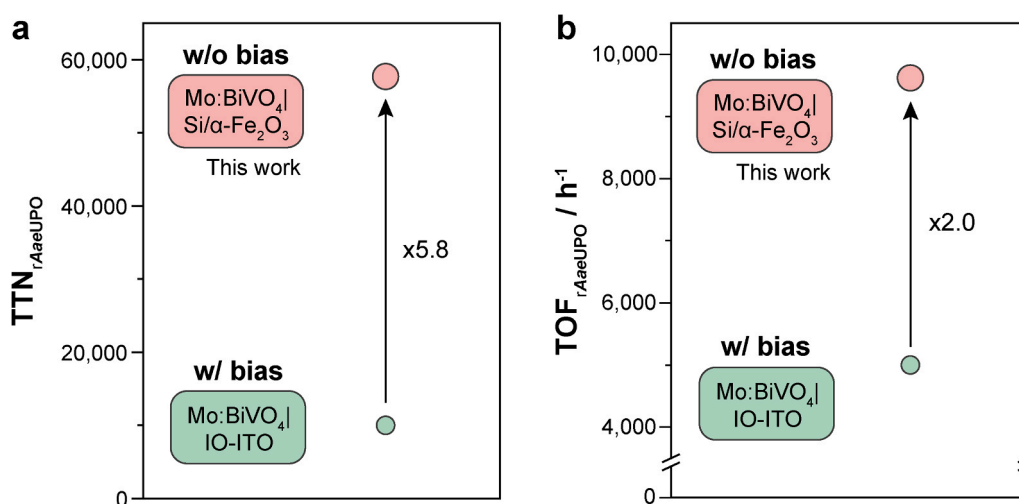


Fig. 5. Comparison of $rAaeUPO$ -hybrid PEC systems for anodic oxyfunctionalization reactions in terms of (a) $TTN_{rAaeUPO}$ and (b) $TOF_{rAaeUPO}$ values. Assembly: $Mo:BiVO_4|IO-ITO$ (green; ref. [24]). IO-ITO, inverse opal-structured indium tin oxide.

accelerate NH_3 production, we synthesized the $\alpha\text{-Fe}_2\text{O}_3$ under O_2 -depleted environments, which increased (i) the number ratio of O_V by 1.33 times and (ii) the rate of NH_3 production by 1.37 times. Concurrently, the photoanodic half-reaction by Mo:BiVO_4 -based energy materials led to the extraction of electrons from H_2O and the transfer of them to the photocathode. To boost the photoanodic H_2O oxidation, we deposited the FeOOH adlayer on the Mo:BiVO_4 photoanode, which gave rise to an increase in charge separation efficiencies (η_surface of 22–53%), a decrease in charge-transfer resistance by up to 1.44 times, a decrease in Tafel slope by 1.3 times, and a suppression of charge recombination. In addition, NH_3 production rate increased with increasing H_2O concentration, which highlighted the role of H_2O as an electron donor for N_2 reduction. When we combined PEC NRR with rAaeUPO -catalyzed oxyfunctionalization reactions, we used Mo:BiVO_4 photoanode that (i) receives holes from NRR reaction, (ii) oxidizes H_2O to H_2O_2 , and (iii) generates rAaeUPO 's the catalytically active oxoferryl heme. Overall, the unbiased NRR platform produced valuable compounds at the photoanodic and photocathodic compartments through enantioselective hydroxylation as well as N_2 reduction.

CRediT authorship contribution statement

Chang Hyun Kim: Conceptualization, Formal analysis, Investigation, Methodology, Visualization, Validation, Writing - original draft, Writing - review & editing. **Jinhyun Kim:** Conceptualization, Formal analysis, Investigation, Methodology, Visualization, Supervision, Validation, Writing - original draft, Writing - review & editing. **Frank Hollmann:** Resources. **Chan Beum Park:** Resources, Supervision, Funding acquisition, Project administration, Writing - original draft, Writing - review & editing.

Declaration of Competing Interest

The authors declare that they have no known competing financial interests or personal relationships that could have appeared to influence the work reported in this paper.

Data availability

Data will be made available on request.

Acknowledgments

This work was supported by the National Research Foundation (NRF) via the Creative Research Initiative Center (grant no. NRF-2015R1A3A2066191), Republic of Korea. We thank Professor Byungha Shin and Dr. Choongman Moon at KAIST for quantifying gas molecules.

Appendix A. Supporting information

Supplementary data associated with this article can be found in the online version at [doi:10.1016/j.apcatb.2023.122925](https://doi.org/10.1016/j.apcatb.2023.122925).

References

- G. Qing, R. Ghazfar, S.T. Jackowski, F. Habibzadeh, M.M. Ashtiani, C.-P. Chen, M. R. Smith, T.W. Hamann, Recent advances and challenges of electrocatalytic N_2 reduction to ammonia, *Chem. Rev.* 120 (2020) 5437–5516.
- B.H.R. Suryanto, K. Matuszek, J. Choi, R.Y. Hodgetts, H.-L. Du, J.M. Bakker, C.S. M. Kang, P.V. Cherepanov, A.N. Simonov, D.R. MacFarlane, Nitrogen reduction to ammonia at high efficiency and rates based on a phosphonium proton shuttle, *Science* 372 (2021) 1187–1191.
- J.G. Chen, R.M. Crooks, L.C. Seefeldt, K.L. Bren, R.M. Bullock, M.Y. Darensbourg, P.L. Holland, B. Hoffman, M.J. Janik, A.K. Jones, M.G. Kanatzidis, P. King, K. M. Lancaster, S.V. Lymar, P. Pfomm, W.F. Schneider, R.R. Schrock, Beyond fossil fuel-driven nitrogen transformations, *Science* 360 (2018), eaar6611.
- B.H.R. Suryanto, H.-L. Du, D. Wang, J. Chen, A.N. Simonov, D.R. MacFarlane, Challenges and prospects in the catalysis of electroreduction of nitrogen to ammonia, *Nat. Catal.* 2 (2019) 290–296.
- Y. Pang, C. Su, G. Jia, L. Xu, Z. Shao, Emerging two-dimensional nanomaterials for electrochemical nitrogen reduction, *Chem. Soc. Rev.* 50 (2021) 12744–12787.
- Y. Liu, J. Lu, Q. Zhang, Y. Bai, X. Pang, S. Wang, H. Bai, W. Fan, Charge-transfer dynamics at a $\text{Ag/Ni-MOF/Cu}_2\text{O}$ heterostructure in photoelectrochemical NH_3 production, *Chem. Commun.* 57 (2021) 8031–8034.
- S. Shang, W. Xiong, C. Yang, B. Johannessen, R. Liu, H.-Y. Hsu, Q. Gu, M.K. H. Leung, J. Shang, Atomically dispersed iron metal site in a porphyrin-based metal-organic framework for photocatalytic nitrogen fixation, *ACS Nano* 15 (2021) 9670–9678.
- A. Banerjee, B.D. Yuhas, E.A. Margulies, Y. Zhang, Y. Shim, M.R. Wasielewski, M. G. Kanatzidis, Photochemical nitrogen conversion to ammonia in ambient conditions with FeMoS -chalcogenides, *J. Am. Chem. Soc.* 137 (2015) 2030–2034.
- Y. Bai, H. Bai, Z. Fang, X. Li, W. Fan, W. Shi, Understanding the Z-scheme heterojunction of $\text{BiVO}_4/\text{PANI}$ for photoelectrochemical nitrogen reduction, *Chem. Commun.* 57 (2021) 10568–10571.
- M. Li, Q. Lu, M. Liu, P. Yin, C. Wu, H. Li, Y. Zhang, S. Yao, Photoinduced charge separation via the double-electron transfer mechanism in nitrogen vacancies $\text{g-C}_3\text{N}_5/\text{BiOBr}$ for the photoelectrochemical nitrogen reduction, *ACS Appl. Mater. Interfaces* 12 (2020) 38266–38274.
- J. Kim, S.H. Lee, F. Tieves, C.E. Paul, F. Hollmann, C.B. Park, Nicotinamide adenine dinucleotide as a photocatalyst, *Sci. Adv.* 5 (2019), eaax0501.
- J. Kim, T.V.T. Nguyen, Y.H. Kim, F. Hollmann, C.B. Park, Lignin as a multifunctional photocatalyst for solar-powered biocatalytic oxyfunctionalization of C–H bonds, *Nat. Synth.* 1 (2022) 217–226.
- J. Kim, J. Jang, T. Hilberath, F. Hollmann, C.B. Park, Photoelectrocatalytic biosynthesis fuelled by microplastics, *Nat. Synth.* 1 (2022) 776–786.
- J. Yoon, H. Jang, M.-W. Oh, T. Hilberath, F. Hollmann, Y.S. Jung, C.B. Park, Heat-fueled enzymatic cascade for selective oxyfunctionalization of hydrocarbons, *Nat. Commun.* 13 (2022) 3741.
- J. Yoon, J. Kim, F. Tieves, W. Zhang, M. Alcalde, F. Hollmann, C.B. Park, Piezobiocatalysis: ultrasound-driven enzymatic oxyfunctionalization of C–H bonds, *ACS Catal.* 10 (2020) 5236–5242.
- J. Kim, Y. Um, S. Han, T. Hilberath, Y.H. Kim, F. Hollmann, C.B. Park, Unbiased photoelectrode interfaces for solar coupling of lignin oxidation with biocatalytic C=C bond hydrogenation, *ACS Appl. Mater. Interfaces* 14 (2022) 11465–11473.
- S. Liu, T. Qian, M. Wang, H. Ji, X. Shen, C. Wang, C. Yan, Proton-filtering covalent organic frameworks with superior nitrogen penetration flux promote ambient ammonia synthesis, *Nat. Catal.* 4 (2021) 322–331.
- M.I. Ahmed, C. Liu, Y. Zhao, W. Ren, X. Chen, S. Chen, C. Zhao, Metal-sulfur linkages achieved by organic tethering of ruthenium nanocrystals for enhanced electrochemical nitrogen reduction, *Angew. Chem. Int. Ed.* 59 (2020) 21465–21469.
- Z. Sun, R. Huo, C. Choi, S. Hong, T.-S. Wu, J. Qiu, C. Yan, Z. Han, Y. Liu, Y.-L. Soo, Y. Jung, Oxygen vacancy enables electrochemical N_2 fixation over WO_3 with tailored structure, *Nano Energy* 62 (2019) 869–875.
- Z. Han, C. Choi, S. Hong, T.-S. Wu, Y.-L. Soo, Y. Jung, J. Qiu, Z. Sun, Activated TiO_2 with tuned vacancy for efficient electrochemical nitrogen reduction, *Appl. Catal. B Environ.* 257 (2019), 117896.
- Y. Zhao, Y. Zhao, R. Shi, B. Wang, G.I.N. Waterhouse, L.-Z. Wu, C.-H. Tung, T. Zhang, Tuning oxygen vacancies in ultrathin TiO_2 nanosheets to boost photocatalytic nitrogen fixation up to 700 nm, *Adv. Mater.* 31 (2019), 1806482.
- K. Chu, F. Liu, J. Zhu, H. Fu, H. Zhu, Y. Zhu, Y. Zhang, F. Lai, T. Liu, A general strategy to boost electrocatalytic nitrogen reduction on perovskite oxides via the oxygen vacancies derived from A-site deficiency, *Adv. Energy Mater.* 11 (2021), 2003799.
- Z. Wang, X. Mao, P. Chen, M. Xiao, S.A. Monny, S. Wang, M. Konarova, A. Du, L. Wang, Understanding the roles of oxygen vacancies in hematite-based photoelectrochemical processes, *Angew. Chem. Int. Ed.* 58 (2019) 1030–1034.
- D.S. Choi, J. Kim, F. Hollmann, C.B. Park, Solar-assisted biorefinery: photoelectrochemical pairing of oxyfunctionalization and hydrogenation reactions, *Angew. Chem. Int. Ed.* 59 (2020) 15886–15890.
- J. Kim, Y.W. Lee, E.-G. Choi, P. Boonmongkolras, B.W. Jeon, H. Lee, S.T. Kim, S. K. Kuk, Y.H. Kim, B. Shin, C.B. Park, Robust $\text{FeOOH/BiVO}_4/\text{Cu(In,Ga)Se}_2$ tandem structure for solar-powered biocatalytic CO_2 reduction, *J. Mater. Chem. A* 8 (2020) 8496–8502.
- K. Kim, C.B. Park, Femtomolar sensing of Alzheimer's tau proteins by water oxidation-coupled photoelectrochemical platform, *Biosens. Bioelectron.* 154 (2020), 112075.
- K.J. McDonald, K.-S. Choi, A new electrochemical synthesis route for a BiOI electrode and its conversion to a highly efficient porous BiVO_4 photoanode for solar water oxidation, *Energy Environ. Sci.* 5 (2012) 8553–8557.
- B. Zhang, L. Wang, Y. Zhang, Y. Ding, Y. Bi, Ultrathin FeOOH nanolayers with abundant oxygen vacancies on BiVO_4 photoanodes for efficient water oxidation, *Angew. Chem. Int. Ed.* 57 (2018) 2248–2252.
- X. Li, W. Fan, Y. Bai, Y. Liu, F. Wang, H. Bai, W. Shi, Photoelectrochemical reduction of nitrate to ammonia over CuPc/CeO_2 heterostructure: understanding the synergistic effect between oxygen vacancies and Ce sites, *Chem. Eng. J.* 433 (2022), 133225.
- F. Wang, Q. Ding, J. Ding, Y. Bai, H. Bai, W. Fan, Frustrated Lewis pairs boosting photoelectrochemical nitrate reduction over $\text{ZnIn}_2\text{S}_4/\text{BiVO}_4$ heterostructure, *Chem. Eng. J.* 450 (2022), 138260.
- J. Kim, S.H. Lee, F. Tieves, D.S. Choi, F. Hollmann, C.E. Paul, C.B. Park, Biocatalytic C=C bond reduction through carbon nanodot-sensitized regeneration of NADH analogues, *Angew. Chem. Int. Ed.* 57 (2018) 13825–13828.
- D. Wang, S.H. Lee, S. Han, J. Kim, N.V.T. Trang, K. Kim, E.-G. Choi, P. Boonmongkolras, Y.W. Lee, B. Shin, Y.H. Kim, C.B. Park, Lignin-fueled

- photoelectrochemical platform for light-driven redox biotransformation, *Green Chem.* 22 (2020) 5151–5160.
- [33] G. Son, J. Kim, C.B. Park, Interference of solvatochromic twist in amyloid nanostructure for light-driven biocatalysis, *ACS Appl. Energy Mater.* 3 (2020) 1215–1221.
- [34] T.-K. Le, J. Kim, N.A. Nguyen, T.H.H. Nguyen, E.-G. Sun, S.-M. Yee, H.-S. Kang, S.-J. Yeom, C.B. Park, C.-H. Yun, Solar-powered whole-cell P450 catalytic platform for C-hydroxylation reactions, *ChemSusChem* 14 (2021) 3054–3058.
- [35] D. Wang, J. Kim, C.B. Park, Lignin-induced CaCO₃ vaterite structure for biocatalytic artificial photosynthesis, *ACS Appl. Mater. Interfaces* 13 (2021) 58522–58531.
- [36] M. Hobisch, M.M.C.H. van Schie, J. Kim, K. Røjkjær Andersen, M. Alcalde, R. Kourist, C.B. Park, F. Hollmann, S. Kara, Solvent-free photobiocatalytic hydroxylation of cyclohexane, *ChemCatChem* 12 (2020) 4009–4013.
- [37] Y.W. Lee, P. Boonmongkolras, E.J. Son, J. Kim, S.H. Lee, S.K. Kuk, J.W. Ko, B. Shin, C.B. Park, Unbiased biocatalytic solar-to-chemical conversion by FeOOH/BiVO₄/perovskite tandem structure, *Nat. Commun.* 9 (2018) 4208.
- [38] Y. Zhang, Z. Xiong, Y. Li, M. Wilson, K.E. Christensen, E. Jaques, P. Hernández-Lladó, J. Robertson, L.L. Wong, Enantioselective oxidation of unactivated C–H bonds in cyclic amines by iterative docking-guided mutagenesis of P450BM3 (CYP102A1), *Nat. Synth.* 1 (2022) 936–945.
- [39] D.C. Miller, S.V. Athavale, F.H. Arnold, Combining chemistry and protein engineering for new-to-nature biocatalysis, *Nat. Synth.* 1 (2022) 18–23.
- [40] M.A. Herrera, D.J. Campopiano, Buy one, get one free, *Nat. Synth.* 1 (2022) 420–421.
- [41] C.-H. Yun, J. Kim, F. Hollmann, C.B. Park, Light-driven biocatalytic oxidation, *Chem. Sci.* 13 (2022) 12260–12279.
- [42] H.S. Soo, Solar-powered biorefinery, *Nat. Synth.* 1 (2022) 192–193.
- [43] D.G. Boucher, S.D. Minter, Making molecules with microplastics, *Nat. Synth.* 1 (2022) 751–752.
- [44] F. Tieves, S.J.-P. Willot, M.M.C.H. vanSchie, M.C.R. Rauch, S.H.H. Younes, W. Zhang, J. Dong, P. GomezdeSantos, J.M. Robbins, B. Bommarius, M. Alcalde, A. S. Bommarius, F. Hollmann, Formate oxidase (FOx) from *aspergillus oryzae*: one catalyst enables diverse H₂O₂-dependent biocatalytic oxidation reactions, *Angew. Chem. Int. Ed.* 58 (2019) 7873–7877.
- [45] W. Zhang, H. Liu, M.M.C.H. van Schie, P.-L. Hagedoorn, M. Alcalde, A.G. Denkova, K. Djanashvili, F. Hollmann, Nuclear waste and biocatalysis: a sustainable liaison? *ACS Catal.* 10 (2020) 14195–14200.
- [46] J.H. Kim, J.S. Lee, Elaborately modified BiVO₄ photoanodes for solar water splitting, *Adv. Mater.* 31 (2019), 1806938.
- [47] S.K. Kuk, J. Jang, J. Kim, Y. Lee, Y.S. Kim, B. Koo, Y.W. Lee, J.W. Ko, B. Shin, J.-K. Lee, C.B. Park, CO₂-reductive, copper oxide-based photobiocathode for Z-scheme semi-artificial leaf structure, *ChemSusChem* 13 (2020) 2940–2944.
- [48] J. Kim, C.B. Park, Shedding light on biocatalysis: photoelectrochemical platforms for solar-driven biotransformation, *Curr. Opin. Chem. Biol.* 49 (2019) 122–129.
- [49] J. Kim, C.B. Park, Artificial photosynthetic biohybrids for CO₂ and N₂ fixation, *Chem. Catal.* 2 (2022) 2425–2427.
- [50] C.H. Lee, J. Kim, C.B. Park, Z-schematic artificial leaf structure for biosolar oxyfunctionalization of hydrocarbons, *ACS Energy Lett.* 8 (2023) 2513–2521.
- [51] Y. Bai, H. Bai, K. Qu, F. Wang, P. Guan, D. Xu, W. Fan, W. Shi, In-situ approach to fabricate BiOI photocathode with oxygen vacancies: understanding the N₂ reduced behavior in photoelectrochemical system, *Chem. Eng. J.* 362 (2019) 349–356.
- [52] M.S. Yu, S.C. Jesudass, S. Surendran, J.Y. Kim, U. Sim, M.-K. Han, Synergistic interaction of MoS₂ nanoflakes on La₂Zr₂O₇ nanofibers for improving photoelectrochemical nitrogen reduction, *ACS Appl. Mater. Interfaces* 14 (2022) 31889–31899.
- [53] A.J. Bard, L.R. Faulkner, *Electrochemical Methods: Fundamentals and Applications*, Wiley, 2000.
- [54] H. Bai, F. Wang, Q. Ding, W. Xie, H. Li, G. Zheng, W. Fan, Construction of frustrated Lewis pair sites in CeO₂-C/BiVO₄ for photoelectrochemical nitrate reduction, *Inorg. Chem.* 62 (2023) 2394–2403.
- [55] J. Kim, C.B. Park, Collaborative catalysis for solar biosynthesis, *Trends Chem.* 5 (2023) 133–146.